ACS APPLIED MATERIALS & INTERFACES

Research Article

www.acsami.org

Controllable Preparation of Core–Shell Au–Ag Nanoshuttles with Improved Refractive Index Sensitivity and SERS Activity

Tingting Bai,[†] Jianfei Sun,[†] Renchao Che,[§] Lina Xu,[†] Chenyue Yin,[†] Zhirui Guo,*[,‡] and Ning Gu*[,†]

[†]State Key Laboratory of Bioelectronics, Jiangsu Key Laboratory for Biomaterials and Devices, School of Biological Science and Medical Engineering, Southeast University, Nanjing 210096, P. R. China

[‡]The Second Affiliated Hospital of Nanjing Medical University, Nanjing 210011, P. R. China

[§]Department of Materials Science and Laboratory of Advanced Materials, Fudan University, Shanghai 200433, P. R. China

Supporting Information

ABSTRACT: Recent studies have conclusively shown that the plasmonic performance of Au nanostructures can be enhanced by incorporating Ag. Here, we developed a simple and robust approach for preparing core–shell Au–Ag nanoshuttles (NSs) using single-crystal Au nanorods (NRs) as cores. Upon tailoring the temperature of the reaction system containing alkaline glycine buffer (pH 8.5), exceptionally monodisperse Au–Ag NSs with sharp tips and tunable shell thickness could be routinely achieved in high yield through an epitaxial growth process. In particular, high-resolution transmission electron microscopy and nitric acid corrosive experiments revealed that the shells of these NSs consisted of a homogeneous Au–Ag alloy, rather than pure Ag or Au as previously reported. It was found that glycine played an important role in determining the final metal contents of the shell by regulating the reduction kinetics. In addition, the obatined Au–Ag NSs with sharp tips were shown to have significantly improved refractive index sensitivity and surface-enhanced Raman scattering activity relative to the original Au NRs, making these materials promising for biomedical applications, such as biosensing and biolabeling.

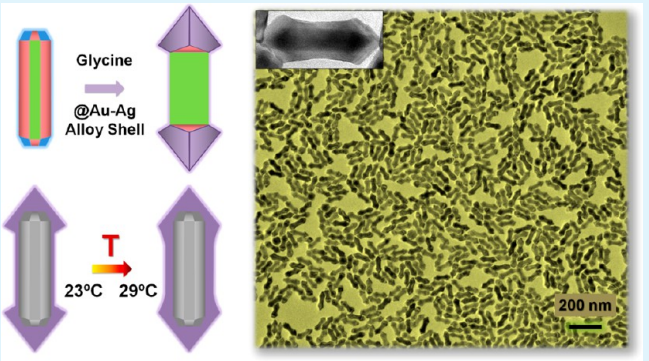

KEYWORDS: *Ag, Au, nanorods, shape control, core–shell structure, refractive index sensitivity, surface-enhanced Raman scattering*

1. INTRODUCTION

Noble metal nanoparticles (NPs), especially Au and Ag NPs, have received extensive attention, mainly owing to their unique localized surface plasmon resonance (SPR) in the visible and near infrared (NIR) regions and wide applications in sensing, catalysis, biomedicine, and so on.[1,2] Numerous investigations have revealed that plasmonic properties of Au and Ag NPs are highly sensitive to their shapes.[3−5] It is also known that Au or Ag NPs with anisotropic shapes exhibit enhanced plasmonic properties.[6] Attempts to control the shape of Au NPs has met with great successes. However, the aqueous-preparation of anisotropic Ag NPs with a uniform shape remains very challenging. Compared with Au NPs, Ag NPs have much stronger and more sensitive SPR, which makes them more competitive in plasmonic sensing and surface-enhanced Raman scattering (SERS) applications.[2] Hence, it is of great importance to develop reliable approaches to prepare anisotropic Ag NPs with good uniformity. To meet this end, an effective solution is to fabricate Au–Ag core–shell nanostructures. Because both Au and Ag are face-centered cubic metals and have close lattice parameters (4.0786 Å for Au and 4.0862 Å for Ag), Ag can grow epitaxially onto a Au NP core under the appropriate conditions.[7] Here, we choose single-crystal Au nanorods (NRs) as cores owing to their unique surface structures, rich plasmonic properties, and ease of preparation.[8] Au NRs have two plasmon bands as a consequence of their one-dimensional anisotropy. One weak band around 510 nm is assigned to the transverse SPR (TSPR), and the other strong band is contributed by a longitudinal SPR (LSPR). Importantly, the LSPR of Au NRs is quite sensitive to the aspect ratio (AR, is the length divided by the diameter). By increasing the AR, the LSPR can be easily tailored from the visible to the NIR region (700−11000 nm), which makes them well-suited for biomedical applications.[9,10] Moreover, the LSPR band of Au NRs shows excellent sensitivity to changes of refractive index, enabling versatile sensing applications.[11,12] In addition, Au NRs were also widely used in SERS owing to their enhanced electric fields at the tips compared with spheres.[13,14]

To date, a variety of Au–Ag nanostructures, such as cylinders,[15] bars,[16] boats,[17] octahedrons,[18] dumbbells,[19] and shuttles[17,20] have been obtained using Au NRs as cores for the epitaxial growth of Ag. The results show that the refractive

Received: November 25, 2013
Accepted: February 17, 2014

   dx.doi.org/10.1021/am405357v | ACS Appl. Mater. Interfaces XXXX, XXX, XXX–XXX

index sensitivity of these core−shell NRs increases with the Ag shell thickness or the aspect ratio.[21,22] On the basis of the improved index sensitivity, a simple and sensitive biosensor can be fabricated to detect molecular binding events in medical and life sciences with a basic spectrophotometer.[23] Furthermore, these core−shell nanostructures can also serve as excellent SERS substrates owing to their significantly higher enhancement factors.[24] Among these nanostructures, Au−Ag nanoshuttles (NSs) with two arrow-headed tips at the ends show the most promise for practical applications. Theoretical calculations predict that, from the combination of tip effects and the Ag component, Au−Ag NSs have a larger extinction cross-section of the LSPR and exhibit much stronger local field enhancements than Au NRs.[20] The theoretical findings from the above studies indicate that Au−Ag NSs can be promising candidates in plasmonic applications, such as optical sensing and SERS detection, and thus systematic experimental verification is quite necessary.

In this work, we developed a convenient and reliable approach for the synthesis of Au−Ag NSs based on modifications of previously reported methods. In our present work, monodisperse Au−Ag NSs with a tunable shell thickness were achieved by simply adjusting the reaction temperature in the glycine buffer. In particular, subsequent structure analysis by high-resolution transmission electron microscopy (HRTEM) and nitric acid corrosive experiments support that these NSs have a homogeneous Au−Ag alloy shell around the Au NR core, rather than the pure Ag or Au shell described in previous documents.[25,26] Moreover, our experimental results revealed that, in addition to being a pH stabilizer, glycine also played an important role in regulating the reduction kinetics. Subsequently, the plasmonic properties of Au−Ag NSs were systematically examined in serial experiments. It was found that these Au−Ag NSs possessed higher refractive index sensitivity as well as excellent SERS activity compared with the original Au NRs.

2. MATERIALS AND METHODS

2.1. Materials. Hexadecyltrimethylammonium bromide (CTAB, 99%) and poly(styrenesulfonate) (PSS, M_w 70,000) were purchased from Sigma. Sodium oleate (NaOL, >97.0%) was purchased from TCI America. Glycine ($C_2H_5NO_2$, ≥ 99.0%) and Tris-base ($C_4H_{11}NO_3$, ≥ 99.5%) was purchased from Biosharp Company (China). 4-Aminothiophenol (4-ATP) was purchased from Aldrich Chemical Company. Hydrogen tetrachloroauric acid ($HAuCl_4{\cdot}4H_2O$, 99%), hydrochloric acid (HCl, 37 %), sliver nitrate ($AgNO_3$), sodium borohydride ($NaBH_4$, 96%), and L-ascorbic acid were all purchased from Shanghai Chemical Reagent Co., Ltd (China). All chemicals were used as received. Deionized water with resistance of 18MΩ was used throughout the experiments. All glassware was cleaned by aqua regia (HCl/HNO_3 in 3:1 ratio by volume).

2.2. Synthesis of Monodisperse Au NRs. Original Au NRs with excellent uniformity were prepared by a binary surfactant assistant, seed-mediated method developed by Ye et al.[27] The gold seeds were prepared by the addition of a freshly prepared, ice-cold $NaBH_4$ solution (0.6 mL, 10 mM) into a solution made by combining $HAuCl_4$ (0.1 mL, 25 mM) and CTAB (9.9 mL, 0.1 M), followed by stirring for 2 min. The seed solution was aged at 30 °C for 2 h allowing for the hydrolysis of unreacted $NaBH_4$. The Au NR growth solution was made by first mixing 100 mL binary surfactant mixture (CTAB 0.037 M, NaOL 0.078 M) with 1.44 mL $AgNO_3$ (10 mM) and 2 mL $HAuCl_4$ (25 mM). The solution was kept at 30 °C for 90 min under stirring (700 rpm). And then, 0.42 mL HCl (37 %, 12.1 M) was introduced to adjust the pH. After the solution was gently mixed, a freshly prepared aqueous ascorbic acid solution (0.16 mL, 0.1 M) was added, and the solution was stirred for 30 s. Finally, 0.08 mL seed solution was injected into the growth solution and kept undisturbed at 30 °C overnight.

2.3. Preparation of bimetallic Core−Shell Au−Ag nanoshuttles. The as-prepared Au NRs were purified by centrifugation at 10000 rcf for 15 min twice. For each kind of Au−Ag NSs, 5 mL of purified Au NRs in 0.1 M CTAB was mixed with 5 mL of 0.2 M glycine acid and 30 μL of 2 M NaOH solutions to obtain a stable pH value of 8.5. Additional $HAuCl_4$ (40 ul, 25 mM) and $AgNO_3$ (0.2 mL, 10 mM) were introduced under vigorously stirring and incubated at different temperatures (23, 25, 27, and 29 °C, respectively). Finally, a portion of ascorbic acid solution (0.2 mL, 0.1 M) was added to the growth solution and stirred for 30 s, and then the whole solution was aged for 1 h. The resulting nanostructures were purified by centrifugation at 7000 rcf for 10 min and denoted as Au−Ag NSs a, Au−Ag NSs b, Au−Ag NSs c, and Au−Ag NSs d in the following paragraphs according to 23, 25, 27, and 29 °C, respectively.

2.4. Nitric Acid Corrosive Experiment. In this experiment, Au@Ag nanobars were used as a control model, which were synthesized by a seed-mediated growth procedure from Okuno et al.[16] 200 μL of 4 M nitric acid was added to 1 mL Au−Ag NSs d and 1 mL Au@Ag nanobars respectively. After 30 min of corrosion, both samples were centrifuged at 7000 rcf for 5 min, redispersed into the water, and then characterized by scanning electron microscopy.

2.5. Refractive Index Sensitivity Measurement. Water−glycerol mixtures of various volume ratios were used to adjust the refractive index of the surrounding medium of nanostructures. The refractive indices of the pure water and glycerol are 1.3334 and 1.4746, respectively. The volume percentage of glycerol in the liquid mixture was varied from 0% to 90% at a step of 10%. The as-prepared Au NRs and Au−Ag NSs were first centrifuged at 10000 rcf for 15 min and 7000 rcf for 10 min, respectively, and then redispersed into the water−glycerol mixture. Extinction spectra of the resulting dispersion solutions were measured. The plasmon shifts relative to the refractive index were plotted, and the refractive index sensitivity was determined by linear fitting. A figure of merit (FOM) is also used to characterize the capability of noble metal nanostructures in plasmonic sensing, which is defined as the ratio of the refractive index sensitivity to the full width at half maximum (FWHM) of the plasmon resonance profile.

2.6. SERS Activity of Au−Ag NSs. The fabrication of Au−Ag NSs monolayer as SERS substrate was conducted through three steps and all the five kinds of NPs (Au NRs, Au−Ag NSs a, Au−Ag NSs b, Au−Ag NSs c, Au−Ag NSs d) were treated with the same procedure. The first step is surface modification of NPs. Twenty milliliters of nanoparticles and Raman reporter molecules (4-ATP) were mixed together in a proportion of 1:10 000 (the molar ratio of nanoparticles to dye molecules) and incubated for 1 h to form the conjugation. The mixture was then centrifuged twice, and the precipitate was redispersed in 20 mL of water. Subsequently, 2 mL PSS (10 mg/L) in 5 mM NaCl was added dropwise, and the mixture solution was kept undisturbed for 1 h. Then, the solution was centrifuged twice to remove excess polyelectrolyte and redispersed in water. All the five NPs were diluted to the same concentration. The second step is functionalization of silicon wafers. The silicon wafers were washed with water, acetone, and ethanol in an ultrasonic bath for 5 min respectively. To increase the coverage of surface hydroxyl groups, the silicon wafers were treated in Piranha solution (3:7 (v/v) H_2O_2/H_2SO_4) for 20 min. Subsequently, these wafers were immersed into a 0.5 wt % PDDA solution for 1 h to make the substrate positively charged. Next, they were rinsed several times with deionized water and dried gently with nitrogen gas. The last step is immobilization. The functionalized wafers were immersed in the five NPs solutions for 36 h, resulting in a monolayer of NPs films on the silicon wafers.

2.7. Instruments. The UV−vis−NIR extinction spectra were recorded by a Shimadzu UV-3600 spectrophotometer in a range of 300−1200 nm. Transmission electron microscopy (TEM) was taken with a JEM-2100EX (JEOL) transmission electron microscope operated at 200 kV. Scanning electron microscopy (SEM) images and the EDS spectra were obtained by a Carl Zeiss ULTRA Plus Field Emission Scanning Electron Microscope. A Renishaw Invia Reflex

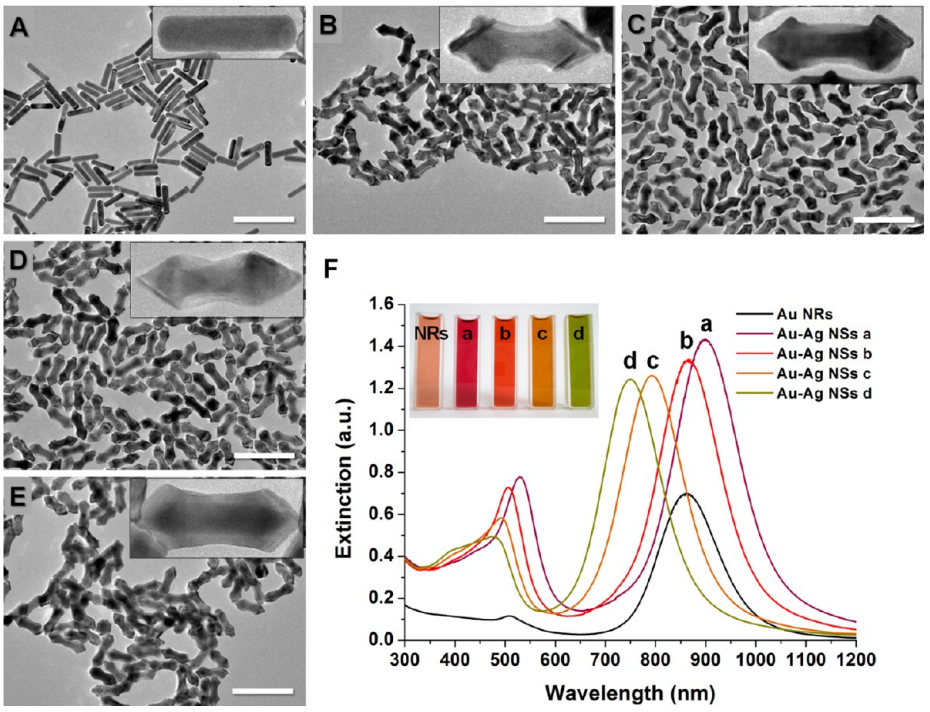

Figure 1. TEM images of the original Au NRs (A) and newly formed Au–Ag NSs grown at 23 (B), 25 (C), 27 (D), and 29 °C (E), respectively. All scale bars are 200 nm. (F) Non-normalized UV–vis–NIR extinction spectra for the original Au NRs and Au–Ag NSs. The inset shows the corresponding photographs of the NPs solutions. All the samples were diluted threefold by deionized water before optical measurements.

Table 1. Physical Dimensions and SPR Bands of Au NRs and Au–Ag NSs[a]

	L (nm)	D_1 (nm)	D_2 (nm)	aspect ratio 1 (L/D_1)	aspect ratio 2 (L/D_2)	λ_T (nm)	λ_L (nm)
Au NRs	83 ± 5	19 ± 1	19 ± 1	4.3	4.3	509	861
Au–Ag NSs a (23 °C)	110 ± 6	38 ± 2	24 ± 2	2.9	4.6	529	899
Au–Ag NSs b (25 °C)	109 ± 6	38 ± 2	25 ± 1	2.9	4.4	506	865
Au–Ag NSs c (27 °C)	108 ± 6	38 ± 2	27 ± 1	2.8	4.0	492	794
Au–Ag NSs d (29 °C)	109 ± 5	39 ± 2	29 ± 2	2.8	3.8	472	748

[a]The descriptors L, D_1, and D_2 are defined in Scheme 1. The descriptors λ_T and λ_L represent the maximum wavelengths of the transverse and longitudinal SPR extinctions, respectively.

Scheme 1. Schematics Illustrating the Formation Process of the Au–Ag NSs: (A) Side View, (B) Top View, (C) Shell Thickness Increasing with the Rise of Temperature, and (D) the Details of Alloy Shell Formation

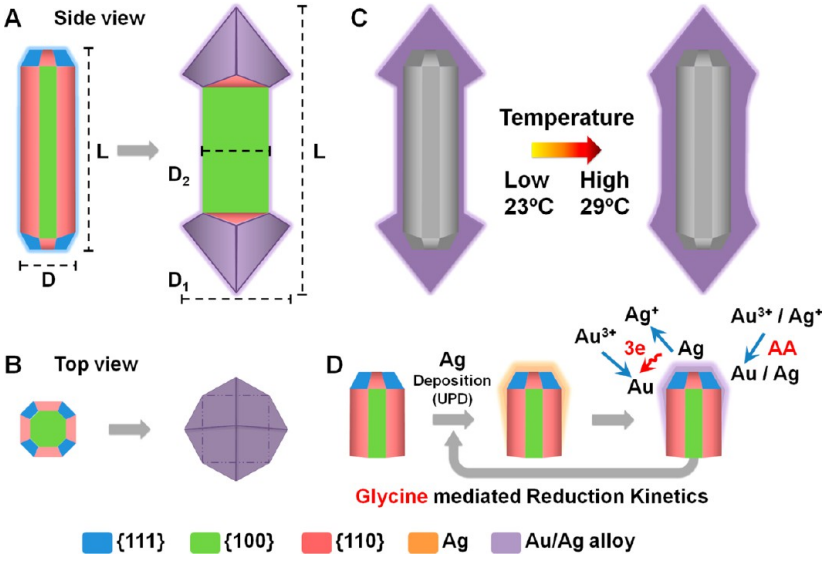

system (equipped with a Peltier-cooled charge-coupled device (CCD) detector and Leica confocal microscope) was used to carry Raman experiments. Samples were excited with 785 nm diode laser under linefocus mode and a grating of 1200 mm^{-1} was used. The laser was focused on the sample surface by using a 50× long working distance objective. The exposure time was 10 s, and the laser power was adjusted to 1%, which was about 1.2 mW. Each SERS spectrum was averaged from 3 measurements. Results were given as means ± the standard deviation (SD). All Raman experiments were carried out at room temperature (~25 °C).

3. RESULTS AND DISCUSSION

3.1. Characterization and UV−vis−NIR Analysis of the Au−Ag NSs. Figure 1A−E show the TEM images of the Au NR templates and resulting Au−Ag NSs. The images clearly indicate that monodisperse Au NRs with negligible shape impurities can be obtained (Figure 1A and Supporting Information Figure S1), making the growth of NSs with excellent size and shape uniformity. Therefore, the NSs can be produced in high-yield with noteworthy size uniformity and shape purity. Figure 1B−E show the TEM images of the Au−Ag NSs prepared at 23, 25, 27, and 29 °C, respectively. All of them have sharp tips at both ends, like a double-headed arrow. The electron density contrast implies that these NSs have a core−shell structure. The thickness of the shell can be increased by raising the temperature of the solution. The length and diameter are measured from the TEM images of 100 particles (Table 1). The descriptors L, D_1, and D_2 are defined in Scheme 1.

Corresponding UV−vis−NIR spectra of these NPs are shown in Figure 1F and the SPR bands are summarized in Table 1. Similar to Au NRs, Au−Ag NSs also exhibit both TSPR and LSPR bands. As shown in Figure 1B−E, metal ions are preferentially deposited at the two ends of the Au NRs and gradually extend to the side when the temperature increases from 23 to 29 °C. Their shapes were effectively controlled by adjusting the reaction temperature. Compared with the change in the length, which is nearly the same after the shape conversion, the increase in diameter (D_2) is more significant and steady (from 24 ±2 nm to 29 ±2 nm). Table 1 summarizes the blue fhift of the LSPR band from 899 to 748 nm, which corresponds to the change in aspect ratio 2 (L/D_2) from 4.6 to 3.8. According to the SPR, the final colors of the four colloid solutions are distinctly different from that of the Au NRs (Figure 1F). For the TSPR band, the position blue-shifts when the diameter of the NSs (D_2) increases. Note that the concentration of the Au NRs and Au−Ag NSs for the UV detection were nearly the same as a result of using an equivalent amount of Au NR seeds. These nanostructures can be almost completely conserved after careful centrifugation, which benefits from their high monodispersity. Thus, we point out that the significant increase in intensity of the SPR bands is ascribed to the formation of the Ag-containing shell on Au NR cores.

HRTEM imaging and the corresponding fast Fourier transformation (FFT) pattern of the selected area were performed to ascertain the crystalline structure of the Au−Ag NSs. Figure 2A shows the HRTEM image of Au−Ag NSs d. The high contrast between the center and periphery clearly reveals the core−shell structure of this NS. The Au NRs were completely embedded into a homogeneous shell, and no pure Au or Ag NPs were observed. This result indicates that the shell cannot be composed of pure Au, in which case the contrast of the core and shell would not exist.[26] The corresponding Fourier

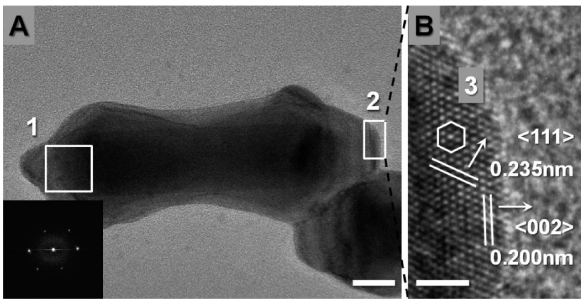

Figure 2. (A) HRTEM image of Au−Ag NSs d. The inset shows the corresponding FFT spot pattern of area 1 demonstrating that the arrow tip is enclosed by {111} facets. (B) Magnification of area 2 in panel A. Scale bars for panels A and B are 10 and 2 nm, respectively.

spectrum obtained from area 1 in the HRTEM image is also shown as an inset. The FFT exhibits a hexagonal symmetry pattern, which is the characteristic of reflections in a face-centered cubic metal (fcc). It strongly suggests that this NS has a single crystalline shell and that the flat surface at the end is a {111} plane. Considering the symmetry of Au NRs, the HRTEM and the FFT pattern show that the two ends of the Au NRs are enclosed by {111} facets. The local enlarged HRTEM image of area 2 at the vertex of the arrow is shown in Figure 2B. In accordance with the FFT results, two types of lattice fringes with interplanar spacings of 0.200 and 0.235 nm are clearly observed, which are attributed to the {002} and {111} planes of Au or Ag. In the bright-field imaging mode of TEM, the electron density contrast is formed by the occlusion and absorption of the electrons in the sample. Thus, the bright field contrast is related to the crystalline structure, thickness, and atomic number of the specimen.[28] Under the same conditions, imaging parameters, and neighboring position at the atomic scale, the brightness of the atomic spots would be determined solely by the atomic number. As marked in area 3, the six spots obviously have a different brightness. Considering the fact that there are only two kinds of metal ions involved in the preparation, it can be concluded that the NSs have an alloy shell, which is a homogeneous solid solution of Au and Ag.

Energy dispersive spectrometer (EDS) analysis and nitric acid corrosive experiments were performed to further investigate of the shell composition. If the shell around the Au NR was composed of pure Au or Ag, the content of the corresponding metal should increase with the growth of the shell. However, EDS analysis on randomly selected areas shows that the average Au/Ag atomic ratio remains almost unchanged (Supporting Information Table S1), which verifies that the shell is not pure Au or Ag. Besides, it is well-known that pure Ag NPs can be dissolved by a strong oxidizing acid like nitric acid.[29] These Au−Ag NSs were then tested using nitric acid together with Au@Ag nanobars (Au NRs coated with a pure Ag shell) as a control. After 30 min of nitric acid corrosion, the shells of the Au@Ag nanobars were nearly corroded, while the profile of Au−Ag NSs d remained almost unchanged (Figure 3). These results agree well with the HRTEM finding that the as-synthesized NSs have an Au−Ag alloy shell. This is contrary to previous reports, in which the shell is composed of pure Ag or Au.[25,26] By combination of these two metals into one NP, the localized SPR can be further enhanced and varied continuously beyond the limits of monometallic Au and Ag NPs. In addition, the Au−Ag alloy is thermodynamically more

dx.doi.org/10.1021/am405357v | ACS Appl. Mater. Interfaces XXXX, XXX, XXX−XXX

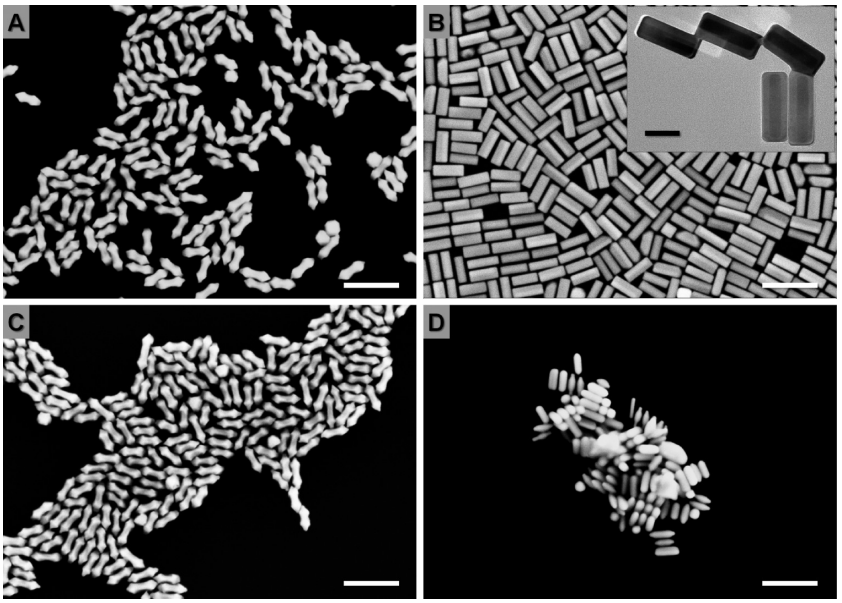

Figure 3. (A) SEM image of Au−Ag NSs d with an alloy shell. (B) SEM image of Au@Ag nanobars (Au NRs coated with a pure Ag shell). The inset shows the corresponding TEM image (scale bar is 40 nm). (C) Au−Ag NSs d after treatment with nitric acid. (D) Au@Ag nanobars after treatment with nitric acid. All scale bars are 200 nm.

stable than pure Au or Ag.[7] All these advantages make the Au−Ag NSs more suitable for plasmonic applications.

3.2. Mediation of the Reduction Kinetics by Glycine. Since it has been documented that amino acids could have the ability to direct the growth of gold nanostructures.[30,31] A series of experiments was carried out to investigate the role of glycine in the reduction kinetics besides the pH stabilization.

The NS growth was performed at varying glycine concentrations (0−0.2 M, 25 °C, pH 8.5). The results show that the Au NRs can grow into NSs at various glycine concentrations or even without glycine (Figure 4A−C). The morphology of the NSs can be seen clearly from the SEM images (Figure 4B). There are four sides around the NS and four symmetrical irregular quadrilaterals at the both tips forming an approximately 45° torsional angle with the sides. Figure 4E shows the extinction spectra of the products grown at varying glycine concentrations up to 0.2 M. It is observed that the SPR intensities of the products obtained using lower glycine concentrations (0−0.02 M) are far lower than those of the products obtained using 0.05−0.2 M glycine. This suggests that the amount of metal ions deposited on the surface of the Au NRs at lower glycine concentrations is smaller than that at higher glycine concentrations. The above results indicate that glycine has little effect on the final morphology of the Au−Ag NSs, but it may have some influence on the deposition of the metal precursors.

Furthermore, Tris, a common pH buffer with an effective pH range between 7 and 9, was also used as a control for preparing Au−Ag NSs. Similar to glycine, NSs could be obtained at varying Tris concentrations (0−0.2 M, 25°C, pH 8.5) without any obvious variation in the morphological architecture (Figure 4D). The average Ag/Au atomic ratio from EDS analysis also proves that Tris can mediate the reduction kinetics during the overgrowth of the Au−Ag NSs (Figure 5). Therefore, our investigation indicates that both of the two buffers have similar effects on the dispersion of metal precursors but to differing degrees, as there is a difference in the Ag/Au atomic ratio between glycine and Tris at low concentration (0.02 M).

3.3. Formation Mechanism of Au−Ag NSs with Alloy Shell. In this study, the synthesis of the original Au NRs is based on the seed-mediated method under the assistance of small amount Ag^+ ions. It has been known that such Au NRs have an single crystal structure and an octagonal cross-section:[32,33] the side facets of the rod are dominated by four {110} and four {100} facets, whereas the ends of the rod are enclosed by {111} and {110} planes (as shown in Scheme 1A and B). In the Ag^+-assisted growth of Au NRs, the preferential underpotential deposition (UPD) of Ag atoms on the Au high-energetic {110} facets prevents Au deposition on them. Thus Au atoms have to deposit onto the {111} facets, resulting in one-dimensional growth in the [100] direction.[34] Furthermore, Xiang et al. in 2008 were the first to demonstrate that the growth mode of the Au NRs could be changed from {110} prevention to preference by adjusting the reaction parameters, including Ag^+/Au^{3+} and AA/Au^{3+} ratios.[25] As a result, more thermodynamically favored shape, such as NSs, can be formed.

In this study, by tuning the molar ratio of Au^{3+}/Ag^+/ascorbic acid to be 1:2:20, we switched the growth mode of metal ions on the surface of Au NRs into {110} preference. Since the only driving force of the formation of arrow-like shape is to minimize the surface energy. On the basis of Xiang et al.'s investigation[25] and the observations we found here, the formation process of the Au−Ag NSs with alloy shell is illustrated as following: under higher Ag^+/Au^{3+} and AA/Au^{3+} ratios, the amount of reduced Ag atoms is higher enough to fully cover all exposed facets of Au NR and thus the preferential UPD deposition of Ag on Au {110} facets would not work. Therefore, the minimization of the surface energy becomes the main driving force to direct the subsequent overgrowth of Au NRs. At the end of Au NR, the four high-energetic {110} facets grow more quickly and disappear finally, while four {111} facets extend and form an arrow-head top. Meanwhile, at the side of the Au NR, metal atoms also deposit more quickly on the {110} facets. As a result, four side {110} facets disappear, leaving the four enlarged {100} facets to form a rod shape with a square cross-section (Scheme 1A and B). During the

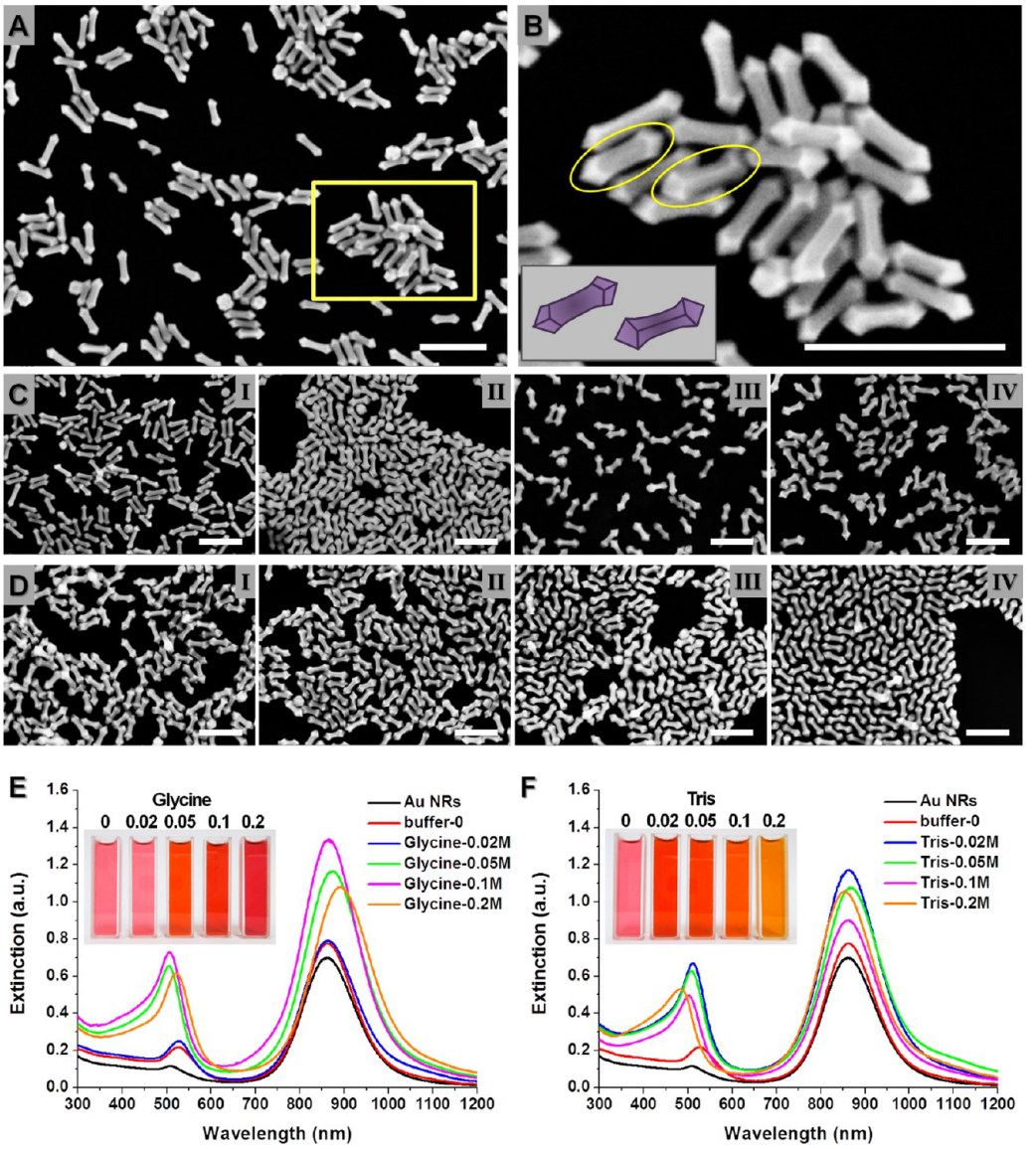

Figure 4. (A) SEM image of Au−Ag NSs b obtained without any buffer solution. (B) Magnification of the selected area from (A) and a sketch of two particles from this image. (C) SEM images of Au−Ag NSs b obtained in glycine solution with different concentrations: (I) 0.02 M, (II) 0.05 M, (III) 0.1 M, and (IV) 0.2 M. (D) SEM images of Au−Ag NSs b obtained in Tris solution with different concentrations: (I) 0.02 M, (II) 0.05 M, (III) 0.1 M, and (IV) 0.2 M. All scale bars are 200 nm. Non-normalized UV−vis−NIR extinction spectra for the original Au NRs and Au−Ag NSs b prepared in glycine (E) and Tris (F) solution with different concentrations.

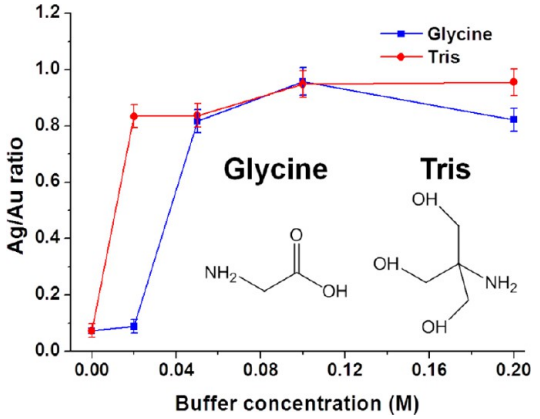

Figure 5. Average Au/Ag atomic ratio of Au−Ag NSs b prepared in glycine and Tris solution with different concentrations.

morphology transformation, new triangular {110} facets appear at the junction between the four side {100} facets and the four {111} facets at the end. Morover, the stronger reducing ability of ascorbic acid at a higher temperature accelerates the shell growth process. Much more metal ions deposit on the emerging triangular {110} facets, leading to increasing of shell thickness (Scheme 1C).

Following reactions are involved in the epitaxial growth process of the alloy shell. Firstly, the Ag^+ is reduced to Ag^0 on the Au facets through UPD deposition. Then Au^{3+} reacts with Ag^0 on the surface of Au NRs. Meanwhile, the free ions can also be reduced by the large amount ascorbic acid. The Au−Ag alloy shell is thus formed as the reduction and in situ galvanic replacement reaction continues. During this process, glycine is found to mediate the reduction kinetics of metal ions and regulate the molar ratio of Au and Ag in the final products, apart from stabilizing the pH value. On the basis of the above

dx.doi.org/10.1021/am405357v | ACS Appl. Mater. Interfaces XXXX, XXX, XXX−XXX

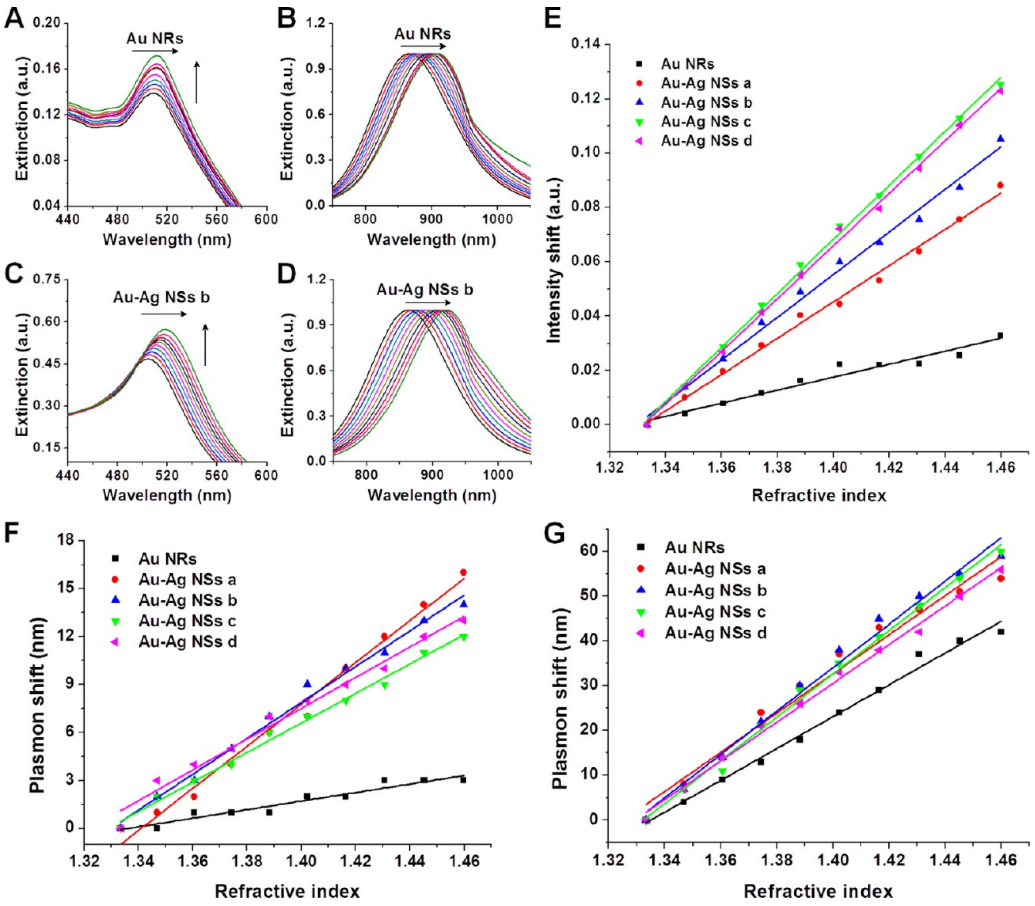

Figure 6. Extinction spectra of Au NRs (A, TSPR; B, LSPR) and Au–Ag NSs b (C, TSPR; D, LSPR) in water–glycerol mixtures of varying compositions. Each extinction spectrum is normalized to its maximum intensity. The arrows indicate the direction of increasing volume percentage of glycerol. Dependence of the TSPR intensity (E), TSPR shift (F), and LSPR shift (G) as a function of the refractive index of the liquid mixture for Au NRs and Au–Ag NSs prepared at the different temperatures.

Table 2. Refractive Index Sensitivities and FOMs of Au NRs and Au–Ag NSs

	λ_T (nm)	λ_L (nm)	FWHM of TSPR (nm)	FWHM of LSPR (nm)	index sensitivity of TSPR (nm/RIU)	index sensitivity of LSPR (nm/RIU)	FOM of TSPR	FOM of LSPR
Au NRs	509	861	72	137	27	355	0.4	2.6
Au–Ag NSs a (23 °C)	529	899	62	148	131	438	2.1	3.0
Au–Ag NSs b (25 °C)	506	865	60	141	112	484	1.7	3.4
Au–Ag NSs c (27 °C)	492	794	67	137	92	483	1.4	3.5
Au–Ag NSs d (29 °C)	472	748	74	131	96	433	1.3	3.3

discussion, it can be summarized that the Au–Ag NSs with alloy shell are obtained by coupling co-reduction and galvanic replacement (Scheme 1D).

3.4. Refractive Index Sensitivities of the Au–Ag NSs. To investigate the refractive index sensitivities of the plasmon resonance peaks of Au–Ag NSs, they were dispersed in binary mixtures of water and glycerol with varying volume percentages of glycerol. The original Au NRs were used as a control to compare the different refractive index sensitivities after the growth of the Au–Ag alloy shell. In all experiments, the highest volume percentage of glycerol was 90%, because pure glycerol is highly viscous. As the refractive index of the solvent mixture increased, all the plasmon peaks shifted to longer wavelengths (Figure 6A–D and Supporting Information Figure S2). The peak wavelengths in different solvents were measured, and the plasmon shifts were determined by taking the difference of plasmon peak wavelengths when the NPs were dispersed in the solvent mixture and in pure water. The refractive indices of the solvent mixtures were calculated according to the Lorenz equation.[12] When the plasmon shifts are plotted as a function of the refractive index of the solvent mixture, we observe an approximately linear dependence for both the TSPR and LSPR. All the plots can be fitted well with a linear approximation, and the slopes of the lines are the refractive index sensitivities (Figure 6F and G). Their values are summarized in Table 2, and the FWHM of the longitudinal peaks and the FOMs are also included.

Table 2 shows that Au–Ag NSs with different aspect ratios exhibit different refractive index sensitivities, which are larger than that of the original Au NRs. In a previous study, the noble

dx.doi.org/10.1021/am405357v | ACS Appl. Mater. Interfaces XXXX, XXX, XXX–XXX

metal NPs were shown to have a larger refractive index sensitivity when they had a larger aspect ratio or a shape with sharper corners.[12] In addition, the refractive index sensitivity also depends on the type of metal, as Ag nanocubes are twice as sensitive to the index change in the surrounding medium as Au nanocubes of nearly the same size.[35] Here, after the overgrowth of the Au−Ag alloy shell on the surface of the Au NRs and the formation of the sharp tips at the ends, both the refractive index sensitivities from the TSPR and LSPR shifts are greater than that of the Au NRs (Figure 6F and G). Especially when the refractive index sensitivity from the TSPR is concerned, a larger difference was found between the Au−Ag NSs and Au NRs compared with that in the LSPR (Figure 6F). However, among the four kinds of NSs, a nonlinear relationship between the refractive index sensitivities and shell thickness was found. Take the index sensitivities from the LSPR as an example (Figure 6G). With the same shape, although the Au−Ag NSs a have the larger aspect ratio and a smaller shell thickness, the index sensitivity is still smaller than that of Au−Ag NSs b, which have a smaller aspect ratio but a thicker shell. This phenomenon can be attributed to the much larger amount of Ag in the alloy shell, since the index sensitivity should decrease with the reduced aspect ratio. This is the result of a combination of two reasons: metal type and aspect ratio. As for Au−Ag NSs b and Au NRs, they have very similar plasmon resonance wavelengths (865 and 861 nm) and aspect ratios (4.4 and 4.3), but they are different in geometry and composition. The measured index sensitivity of Au−Ag NSs b is ∼1.4-fold larger than that of Au NRs. Combined with the previous experimental study (sharper apexes increase the index sensitivity)[12] and finite-difference time-domain (FDTD) calculations,[20] we can infer that the increasing of Au−Ag NSs b index sensitivity by a large margin is caused by the combination of the sharp-tip geometry and the high quantity Ag in the shell. Similarly, the aspect ratios of Au−Ag NSs c and Au−Ag NSs d are greatly decreased, while their index sensitivities decrease only slightly. As shown by previous reports and our results, the metal type, aspect ratio and shape are all influencing factors. However, it is hard to ascertain which factor is dominant in this study, because they are codependent and change together when the Au NRs grow into NSs. And more studies are still needed yet to solve this issue.

The FOMs of the different SPRs of Au−Ag NSs listed in Table 2 were also determined from the measured index sensitivities and the resonance peak widths in the extinction spectra. The peak widths for the determination of the FOMs were obtained by fitting the extinction spectra with multiple Gaussian functions.[35] Although the TSPRs of these NPs have narrower peak widths than the of LSPRs, their FOMs are very small, owing to their relatively lower index sensitivities. In contrast, the LSPRs of these NPs possess larger FOMs because of their higher index sensitivities. It is worth mentioning that the FOMs of the NSs are all above 3.0, which is greater than that of the Au NRs. The possession of larger index sensitivities and FOMs makes the Au−Ag NSs appealing for use in highly sensitive plasmonic sensors. Besides the index sensitivity and FOM, it is very interesting that the intensities of all the TSPRs from the normalized UV−vis spectra gradually increase as the refractive index of the solvent increases (Figure 6A and C and Supporting Information Figure S2A, C, and E). When the intensity shifts of the extinction spectra were plotted as a function of the refractive index, an approximately linear dependence was also observed (Figure 6E). Figure 6E clearly shows a gradual increase and variation in the slope of the TSPR intensity shifts with an increase in the alloy shell thickness. Therefore, the slope of these curves can also be used to determine the refractive index sensitivity of the NPs, which is proportional to the alloy shell thickness.

3.5. SERS Enhancement of the Au−Ag NSs. To study the SERS enhancement of the Au−Ag NSs compared with Au NRs, a monolayer film of these metallic NPs was prepared by a chemical assembly method using electrostatic interactions. The cationic polyelectrolyte PDDA was used as an adhesive layer for the NPs on the surface of a silicon substrate. A negatively charged anionic polyelectrolyte, PSS, is needed to modify the NPs as they are capped by a positively charged bilayer of CTAB. Supporting Information Figure S3 shows the extinction spectra of the Au−Ag NSs (a, b, c, d)/4-ATP/PSS and Au NRs/4-ATP/PSS. A slight red-shift is observed in the spectra of all the NSs except the NRs, which exhibit nearly no shift. After coating, the NPs can still disperse uniformly in water without aggregation. Supporting Information Figure S4 shows the SEM images of the surface morphologies of the monolayers of metallic NPs. It can be seen clearly that both the NSs with different shell thicknesses and the NRs can assemble uniformly on the substrate. In particular, most of the NPs exist separately with a large enough interparticle distance, to allow an investigation on the SERS effects of the individual NSs.

The Au−Ag NSs have two sharp tips at both ends and a large amount of Ag in the alloy shell. According to theoretical and experimental studies, Ag NPs are more SERS-active than Au NPs, and the NSs were expected to have larger local electromagnetic field enhancements. The Au−Ag NSs should therefore be more advantageous than Au NRs when applied in Raman sensing because of their larger SERS enhancement. The SERS spectra of the 4-ATP molecules adsorbed on the monolayers of metallic NPs are shown in Figure 7A. A SERS enhancement with the a_1 vibrational modes of 4-ATP on the Au NRs monolayer, at 1591 (C−C) and 1083 cm^{-1} (C−S), is observed. The band at 394 cm^{-1} represents the C−S bending vibration. The observed peak positions of 4-ATP agree with the values reported in the literature.[36] Relative to the spectrum obtained from the Au NRs, there are slight frequency shifts and changes in the relative intensity of some bands. For example, the two obviously enhanced peaks obtained from Au−Ag NSs d, at 1598 cm^{-1} (C−C) and at 1083 cm^{-1} (C−S), were slightly shifted. An apparent stronger intensity of the SERS spectrum of 4-ATP on the surface of the NSs was obtained, which indicates that the Au−Ag NSs can be used as a good SERS substrate. As a characteristic of 4-ATP, the peak at 1083 cm^{-1} exhibits the highest intensity and was used to compare the enhancement of the different NP monolayers. As shown in Figure 7B, the increase of the alloy shell thickness leads to a strong enhancement of the SERS intensity. Our findings show that NSs with a Au−Ag alloy shell tend to be more SERS active than pure Au NRs and more stable than Ag NPs, and thus they provide an advantage when measuring low concentrations of analyte.

4. CONCLUSIONS

In summary, we have developed a facile approach for high-quality Au−Ag NSs with two sharp tips at both ends using highly monodisperse Au NRs as cores. By simply adjusting the reaction temperature in a glycine buffer, we could finely modulate the shell thickness of the Au−Ag NSs to achieve tunable plasmonic properties over a wide range. Subsequent investigations indicated that these Au−Ag NSs have more

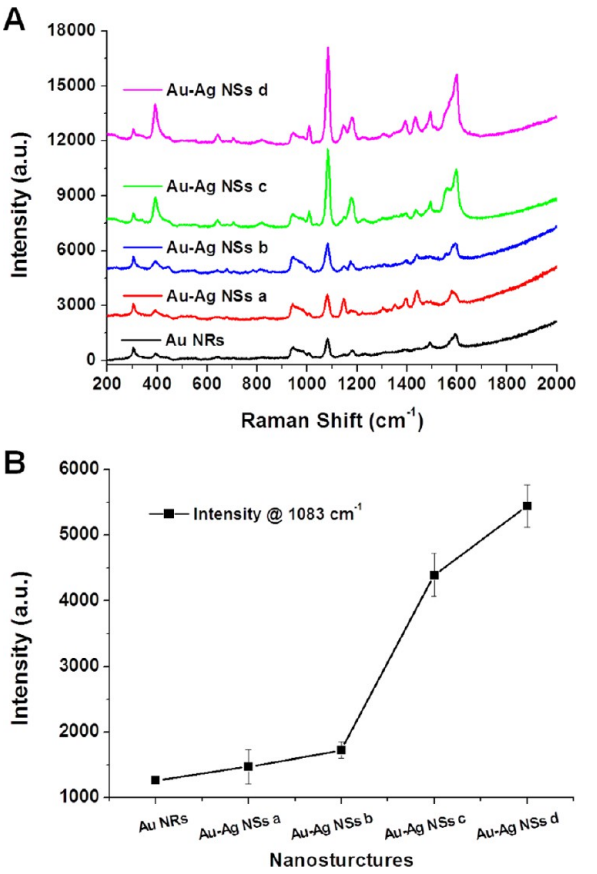

Figure 7. (A) SERS spectra of 4-ATP molecules on the self-assembled monolayers of Au NRs and various Au–Ag NSs, which are marked beside each curve. (B) Measured SERS intensity of the 4-ATP characteristic band at 1083 cm^{-1}.

stable Au–Ag alloy shells, the formation of which can be ascribed to a seed-mediated co-reduction mechanism driven by thermodynamics and the mediation of the reduction kenitics by glycine. Because of their highly anisotropic shape and bimetallic composition, these Au–Ag NSs exhibited higher refractive index sensitivities and excellent SERS enhancements compared to the original Au NRs. Therefore, the Au–Ag NSs are expected to have wide applications in biosensing and biolabeling. In addition, these Au–Ag NSs also have potential for use in imaging, hyperthermia therapy, catalysis and chemical-specific optical sensing.

■ ASSOCIATED CONTENT

Supporting Information

Additional UV–vis–NIR spectra and SEM images. This material is available free of charge via the Internet at http://pubs.acs.org.

■ AUTHOR INFORMATION

Corresponding Authors

*Fax: +86 25 83738572. E-mail: zhiruiguo2009@gmail.com.
*Fax: +86 25 83272460. E-mail: guning@seu.edu.cn.

Notes

The authors declare no competing financial interest.

■ ACKNOWLEDGMENTS

We acknowledge the support from the National Key Basic Research Program of China (2011CB933503), the National Natural Science Foundation of China (61127002, 21273002), the Open Project Program (KF-GN-201107), Jiangsu province science and technology support project (BE2013725), and the Basic Research Program of Jiangsu Province (BK2011036, BK2011590). A project funded by the Priority Academic Program Development of Jiangsu Higher Education Institutions.

■ REFERENCES

(1) Daniel, M.-C.; Astruc, D. *Chem. Rev.* **2004**, *104*, 293–346.
(2) Rycenga, M.; Cobley, C. M.; Zeng, J.; Li, W.; Moran, C. H.; Zhang, Q.; Qin, D.; Xia, Y. *Chem. Rev.* **2011**, *111*, 3669–3712.
(3) Burda, C.; Chen, X.; Narayanan, R.; El-Sayed, M. A. *Chem. Rev.* **2005**, *105*, 1025–1102.
(4) Xia, Y.; Halas, N. J. *MRS Bull.* **2005**, *30*, 338–348.
(5) Liz-Marzán, L. M. *Langmuir* **2006**, *22*, 32–41.
(6) Sau, T. K.; Rogach, A. L.; Jäckel, F.; Klar, T. A.; Feldmann, J. *Adv. Mater.* **2010**, *22*, 1805–1825.
(7) Sun, Y.; Xia, Y. *Nano Lett.* **2003**, *3*, 1569–1572.
(8) Lohse, S. E.; Murphy, C. J. *Chem. Mater.* **2013**, *25*, 1250–1261.
(9) Huang, X.; El-Sayed, I. H.; Qian, W.; El-Sayed, M. A. *J. Am. Chem. Soc.* **2006**, *128*, 2115–2120.
(10) Ding, H.; Yong, K.-T.; Roy, I.; Pudavar, H. E.; Law, W. C.; Bergey, E. J.; Prasad, P. N. *J. Phys. Chem. C* **2007**, *111*, 12552–12557.
(11) Yu, C.; Irudayaraj, J. *Anal. Chem.* **2007**, *79*, 572–579.
(12) Chen, H.; Kou, X.; Yang, Z.; Ni, W.; Wang, J. *Langmuir* **2008**, *24*, 5233–5237.
(13) Wei, W.; Chen, K.; Ge, G. *Adv. Mater.* **2013**, *25*, 3863–3868.
(14) Wang, C.; Chen, Y.; Wang, T.; Ma, Z.; Su, Z. *Adv. Funct. Mater.* **2008**, *18*, 355–361.
(15) Becker, J.; Zins, I.; Jakab, A.; Khalavka, Y.; Schubert, O.; Sönnichsen, C. *Nano Lett.* **2008**, *8*, 1719–1723.
(16) Okuno, Y.; Nishioka, K.; Kiya, A.; Nakashima, N.; Ishibashi, A.; Niidome, Y. *Nanoscale* **2010**, *2*, 1489–1493.
(17) Park, K.; Drummy, L. F.; Vaia, R. A. *J. Mater. Chem.* **2011**, *21*, 15608–15618.
(18) Sánchez-Iglesias, A.; Carbó-Argibay, E.; Glaria, A.; Rodríguez-González, B.; Pérez-Juste, J.; Pastoriza-Santos, I.; Liz-Marzán, L. M. *Chem.—Eur. J.* **2010**, *16*, 5558–5563.
(19) Huang, C.-C.; Yang, Z.; Chang, H.-T. *Langmuir* **2004**, *20*, 6089–6092.
(20) Li, M.; Zhang, Z.; Zhang, X.; Li, K.; Yu, X. *Opt. Express* **2008**, *16*, 14288–14293.
(21) Fu, Q.; Zhang, D. G.; Yi, M. F.; Wang, X. X.; Chen, Y. K. *J. Opt.* **2012**, *14*, 085001–086005.
(22) Lee, K.-S.; El-Sayed, M. A. *J. Phys. Chem. B* **2006**, *110*, 19220–19225.
(23) Huang, H.; Liu, X.; Liao, B.; Chu, P. K. *Plasmonics* **2011**, *6*, 1–9.
(24) Fernanda Cardinal, M.; Rodriguez-Gonzalez, B.; Alvarez-Puebla, R. A.; Perez-Juste, J.; Liz-Marzan, L. M. *J. Phys. Chem. C* **2010**, *114*, 10417–10423.
(25) Xiang, Y.; Wu, X.; Liu, D.; Feng, L.; Zhang, K.; Chu, W.; Zhou, W.; Xie, S. *J. Phys. Chem. C* **2008**, *112*, 3203–3208.
(26) Park, K.; Vaia, R. A. *Adv. Mater.* **2008**, *20*, 3882–3886.
(27) Ye, X.; Zheng, C.; Chen, J.; Gao, Y.; Murray, C. B. *Nano Lett.* **2013**, *13*, 765–771.
(28) Midgley, P.; Weyland, M. *Ultramicroscopy* **2003**, *96*, 413–431.
(29) Özmetin, C.; Copur, M.; Yartasi, A.; Kocakerim, M. *Chem. Eng. Technol.* **2000**, *23*, 707–711.
(30) Shao, Y.; Jin, Y.; Dong, S. *Chem. Commun.* **2004**, *9*, 1104–1105.
(31) Kou, X.; Zhang, S.; Yang, Z.; Tsung, C.-K.; Stucky, G. D.; Sun, L.; Wang, J.; Yan, C. *J. Am. Chem. Soc.* **2007**, *129*, 6402–6404.
(32) Wang, Z. L.; Mohamed, M. B.; Link, S.; El-Sayed, M. A. *Surf. Sci.* **1999**, *440*, L809–L814.

(33) Smith, D. K.; Miller, N. R.; Korgel, B. A. *Langmuir* **2009**, *25*, 9518−9524.
(34) Liu; Guyot-Sionnest, P. *J. Phys. Chem. B* **2005**, *109*, 22192−22200.
(35) Lee, Y. H.; Chen, H.; Xu, Q.-H.; Wang, J. *J. Phys. Chem. C* **2011**, *115*, 7997−8004.
(36) Hu, X.; Cheng, W.; Wang, T.; Wang, Y.; Wang, E.; Dong, S. *J. Phys. Chem. B* **2005**, *109*, 19385−19389.